OPTICS

High-brightness lasing at submicrometer enabled by droop-free fin light-emitting diodes (LEDs)

Babak Nikoobakht[1]*, Robin P. Hansen[1], Yuqin Zong[1], Amit Agrawal[1,2], Michael Shur[3], Jerry Tersoff[4]

"Efficiency droop," i.e., a decline in brightness of light-emitting diodes (LEDs) at high electrical currents, limits the performance of all commercial LEDs and has limited the output power of submicrometer LEDs and lasers to nanowatts. We present a fin *p-n* junction LED pixel that eliminates efficiency droop, allowing LED brightness to increase linearly with current. With record current densities of 1000 kA/cm^2, the LEDs transition to lasing, with brightness over 20 μW. Despite a light extraction efficiency of only 15%, these devices exceed the output power of any previous electrically driven submicrometer LED or laser pixel by 100 to 1000 times while showing comparable external quantum efficiencies. Modeling suggests that spreading of the electron-hole recombination region in fin LEDs at high injection levels suppresses the nonradiative Auger recombination processes. Further refinement of this design is expected to enable a new generation of high-brightness LED and laser pixels for macro- and microscale applications.

INTRODUCTION

Since the breakthroughs in GaN blue light-emitting diode (LED) technology (*1*–*3*) and the subsequent realization of white LEDs, great progress has been made in wide bandgap (WBG) semiconductor LED lighting for general illumination (*4*), display (*5*), and many other applications (*6*), including biological sensing, surface disinfection and sterilization (*7*), visible-blind photodetectors (*8*), acoustic optoelectronics (*9*), and terahertz electronics (*10*). In emerging miniaturized applications, these materials are heavily investigated for nanoscale LEDs and lasers for on-chip optical communication (*11*), chemical sensing (*12*, *13*), high-definition displays (*5*), and visible light communication (*14*) to name a few. Impressive developments have been achieved in electrically pumped nanoLEDs and low-threshold nanolasers based on photonic crystals (*15*, *16*), nanopillars (*17*, *18*), or nanowires (*19*, *20*) with output powers in the pico- to nanowatt range (*11*). However, these nanoscale light sources still have too low power for most practical applications (*11*). Like all LED technology, they are limited by "efficiency droop," which is the decline in internal quantum efficiency (IQE) with increasing current density (*21*). In addition, there is a thermal decrease in IQE with increasing current due to heat generation at the junction. In planar LEDs, the IQE is shown to decrease by 30% as junction temperature increases from 23° to 177°C (*22*–*24*). As a result of these effects, measurements in nanoscale LEDs show a rollover of the IQE at injected currents as low as 0.3 to 4 mA (*17*, *25*–*27*).

The mechanisms causing droop are among the most heavily investigated topics in WBG materials. Efficiency droop has been linked to Auger recombination (*28*, *29*), phase-space filling (*30*), stimulated emission (*31*, *32*), delocalization-activated nonradiative recombination (*33*–*35*), and incomplete carrier localization (*36*, *37*). Here, we report a *p-n* heterojunction ZnO-GaN fin LED that inherently does not show efficiency droop even at record high current densities. Direct measurements and modeling show that the carrier loss mechanisms due to nonradiative pathways stay well controlled, which we attribute to the fin architecture. Measurement of the total spectral radiant flux shows that output power of the fin LED pixels increases linearly with drive current. Results show that the charge carrier radiative recombination efficiency is high enough to cope with the optical loss and allow lasing in the fin cavity at notably high current densities and temperatures.

RESULTS AND DISCUSSION

The fin LED architecture shown in Fig. 1A includes a lateral ZnO nanofin (1) epitaxially grown on *p*-GaN. ZnO has a wurtzite crystal structure and a bandgap (E_g) of 3.36 eV, similar to that of GaN (E_g = 3.43 eV). However, it has a considerably larger exciton binding energy of about 60 meV (relative to 24 meV in GaN) (*38*), making it more effective for high-temperature light sources and optoelectronics resistant to radiation damage. The fins are grown via an Au-catalyzed vapor-liquid-solid (VLS) growth process that is directed on the surface (*39*), where the Au nanodroplets formed at the periphery of the catalyst pattern nucleate the nanofins (Fig. 1B). On *c*-GaN, a ZnO fin grows upright in the [0001] direction and laterally in the *m*-direction with an average width of about 160 nm and length of about 5 μm or longer. A ZnO fin could have one or two large nonpolar ($11\bar{2}0$) side facets (*39*). Fabrication of a fin LED is completed by connecting the *n*-type fin to the *n*-metal electrode. We used a "facet-selective contact" method (Fig. 1, C and D), in which one of the fin side facets is first passivated with a dielectric layer (2), deposited at an angle (Fig. 1D). The other nonpolar side facet remains accessible to receive the *n*-contact metal electrode (3), as presented in Fig. 1E. The side facet–selective contact method also results in the facile formation of clean metal-semiconductor interfaces, as shown in the cross-section of Fig. 1F. The fabrication strategy that allows large-area low-resistance contacts to fin LEDs will be described elsewhere.

Figure 2 presents the optical image (A) of a single fin LED pixel (under operation) and its magnified scanning electron microscope (SEM) image (B) delineating different device parts such as metal contacts. Electrically addressable fin LED pixels are fabricated using

[1]National Institute of Standards and Technology, Gaithersburg, MD 20899, USA. [2]Maryland NanoCenter, University of Maryland, College Park, MD 20742, USA. [3]Rensselaer Polytechnic Institute, 8th Street, Troy, NY 12180, USA. [4]IBM T. J. Watson Research Center, Yorktown Heights, NY 10598, USA.
*Corresponding author. Email: babakn@nist.gov

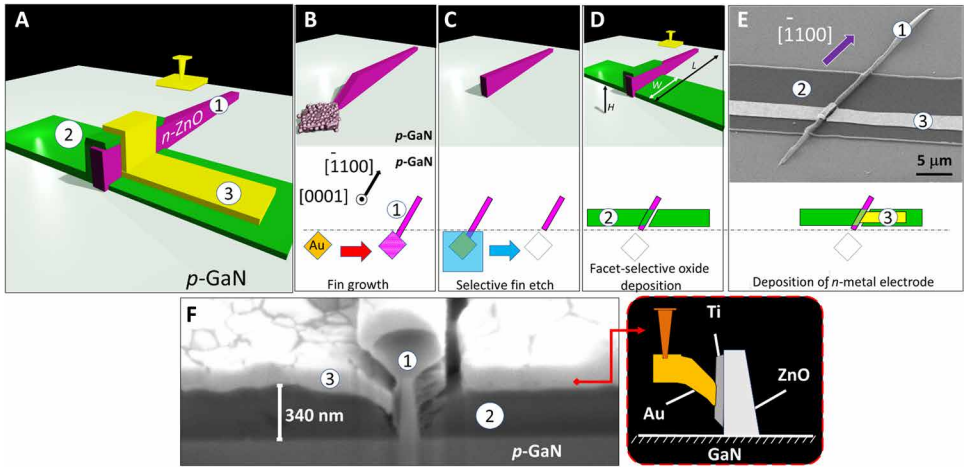

Fig. 1. Architecture and fabrication steps of *n*-ZnO fin LED on *p*-GaN. (**A**) A fin LED pixel includes *n*-ZnO fin (1), isolating dielectric material (2), and *n*-metal contact (3). (**B**) Surface-directed ZnO fin epitaxially grown on *c*-plane GaN from an Au catalyst pattern via surface-directed VLS growth process. (**C**) Isolated fins are formed by removing the initial catalyst site via photolithography and wet etch. (**D**) One of the fin side facets is passivated via photolithography and angled-oxide deposition. The open facet has an approximate area of $H \times W$, where "*H*" is height and "*W*" is width. The maximum length of *W* can be the fin length (*L*). (**E**) The open side of the fin receives the *n*-metal contact. (**F**) Electron micrograph of cross-section of a fin LED. Inset schematically shows the fin, *n*-metal contact, and GaN substrate.

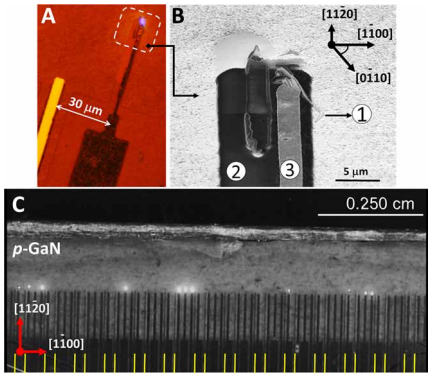

Fig. 2. A fin LED pixel. (**A**) Optical image of a LED pixel containing a single fin. The yellow electrode (true color) in the left side is the *p*-metal contact. The marked area shows the fin LED under forward bias. Its SEM image is shown in (**B**), highlighting different layers of the pixel and the GaN crystallographic directions. (**C**) Optical image of a linear array of fin LED pixels. The bright spots represent fin LED pixels that are ON. The yellow lines highlight the position of *p*-contact electrodes relative to the *n*-contacts. In the image, the ZnO fin grow direction is in $[1\bar{1}00]_{GaN}$.

standard photolithography. Figure 2C shows an example of a linear array. In this optical image, fin LED pixels containing 1 to 10 fins are spaced 120 μm apart across a 1-cm range. For better current spreading in the *p*-GaN layer, the *p*-contact microelectrodes (yellow highlights) are spaced about every 170 and 300 μm.

Fin LED pixels are so bright that the individual pixels in the wire-bonded linear array can be directly measured in front of a metrology-grade charge-coupled device (CCD) array spectroradiometer with no focusing optics (Fig. 3A). Using this setup, the total spectral radiant fluxes of individual fin LED pixels were measured at different drive currents. Figure 3B shows a series of representative electroluminescence (EL) spectra obtained from a pixel containing eight nanofins (pixel #17), with an average fin length of 5 μm and height of 1 μm. Two peaks are visible, at 3.37 (368 nm) and 3.28 eV (378 nm), as current is increased. These wavelengths agree with the neutral donor bound exciton (D^0X) recombination in ZnO. Observation of these two peaks at room temperature and their agreement with the room temperature cathodoluminescence (CL) data (filled spectrum) highlights the high quality of the ZnO fins and underlines the low concentration of the donor states relative to that typically observed in unintentionally *n*-doped ZnO nanowires (*38*, *40*). A low concentration of the donor states is also evidenced by the flow of holes from *p*-GaN to the *n*-ZnO and their recombination in the ZnO fin. Fitting these spectra gives a full width at half maximum (FWHM) of only 5 and 18 nm for these two peaks, demonstrating the low defect density of the fins. In the EL spectra, at lower injection currents, the appearance of the red shoulder at about 2.96 eV (420 nm) indicates radiative *e*-*h* recombination in GaN, due to the slow movement of holes toward the *p*-*n* interface. As the drive current increases, the intensity of the ultraviolet (UV) EL peaks at 3.37 eV (368 nm) and 3.28 eV (378 nm) continues to rise, while the *e*-*h* recombination in GaN is suppressed.

To further explore the impact of drive current on the output power and spectral properties of fin LEDs, the total spectral radiance flux (W/nm) of a pixel (#50) containing five fins was investigated up to 100 mA (the limit of the measurement setup) using the integrating sphere described in Fig. 3A. The pixel was operated under a direct current bias during the operation times of 50, 25, 10, 5, 2.5, 1, and 0.5 s and for the current range of 1, 2, 5, 10, 20, 50, and 100 mA, respectively. After each measurement, a 10-min rest time ensured that the fin LED reached the equilibrium temperature of 25 (±0.1)°C established by a temperature-controlled stage. The total radiant flux–current graph of Fig. 3C (dark circles) shows a nearly linear increase in the output power. For instance, 100 times increase in the injected current results in an about 108 times increase in the optical power for the pixel, i.e., 1 μW at 100 mA. This observation indicates that, at high currents, the carrier loss due to nonradiative events is well controlled. The loss of carriers inside the active region at high injected currents is one of the main processes that promote the efficiency droop. As the current increases, the rise of the intense UV EL peaks

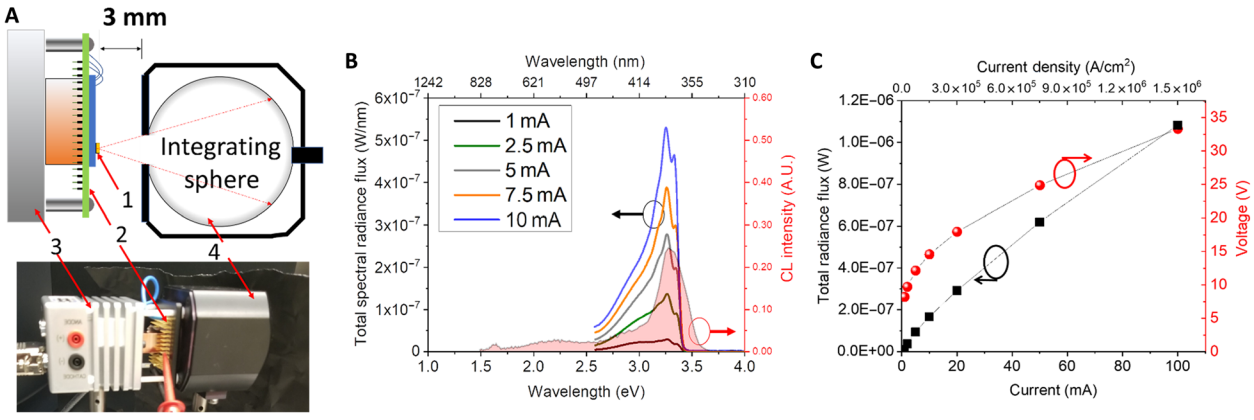

Fig. 3. EL and output power of fin LEDs. (**A**) Wire-bonded array of fin LEDs mounted in front of a 44-mm-diameter integrating sphere, which is connected to a calibrated metrology-grade CCD array spectroradiometer using an optical fiber bundle. Fin LED pixel (1), chip carrier (2) mounted on a stage (3), and detector (4). Photo credit: Babak Nikoobakht, National Institute of Standards and Technology. (**B**) Total spectral radiance flux (W/nm) of a representative pixel containing eight fin LEDs as the injection current is increased from 1 to 10 mA. Each spectrum is an average of five measurements with a total time of 325 s. Two intense UV emission peaks appear at 368.5 nm (3.369 eV) and 378.5 nm (3.280 eV). The filled spectrum is the CL of a single ZnO fin at 2 keV. A.U., arbitrary units. (**C**) Total output power (left axis) and voltage-current data (right axis) of a representative pixel containing three fin LEDs at different injection currents of 1 to 100 mA. Expanded uncertainty in power measurement is less than 5%, with coverage factor of $k = 2$.

in the range of 3.37 to 3.18 eV (368 to 390 nm) in Fig. 4A shows that the radiative recombination occurs in the ZnO fin, as shown in the band structure of the ZnO-GaN heterojunction (Fig. 4B). In contrast to other types of LEDs, at high injection currents, the flow of electrons (electron leakage) to the *p*-GaN is not observed in fin LEDs. Such a leakage is an important factor in promoting the droop effect at high current densities (*41*).

As current is raised, the EL UV peaks redshift in an approximately linear fashion (see Fig. 4C). For instance, the 3.37-eV (368.5 nm) peak redshifts about 27 meV (3 nm) at 10 mA and 144 meV (17 nm) at 100 mA, reaching 3.22 eV (385.4 nm). This shift is due to the junction temperature increase. The temperature-dependent EL studies of the fin LEDs also show a linear redshift in the UV peak position (fig. S1). On the basis of these measurements, the 144-meV redshift in the fin LED corresponds to a marked rise in the junction temperature to approximately 340°C during its 0.5-s operation. At the low injection current of 2 mA, the temperature-dependent EL analysis from 25° to 110°C (Fig. 4D) shows no notable variation in the charge recombination in the ZnO fin. Hence, the defect-related Shockley-Read-Hall (SRH) nonradiative carrier recombination in the fin is minor. Meanwhile, as the as temperature is raised, a gradual suppression of *e-h* recombination in GaN is observed (fig. S2). These results underline the tolerance of ZnO fin LEDs to nonradiative recombination processes, both at low and high current densities. The resilience of fin LEDs to high temperature is also in line with a higher exciton binding energy of ZnO compared to GaN.

The fin LED pixels with the fin numbers smaller than five, consistent with pixels with more fins, show that their total radiant flux (output optical power) grows linearly with injected current and, at 50 mA, reaches 1 to 3.5 μW, as shown for four randomly selected pixels in Fig. 4E. Taking into account the active area of a fin LED, these values correspond to output power densities ranging from 16 to 235 W/cm^2 (Supplementary Materials). Note that, at 50 mA, fin LED pixels receive substantial current densities in the range of 0.45 to 2.2 MA/cm^2, depending on the number of their fins (Supplementary Materials), which highlights their advantageous large side facets for current injection. Nanowire-based LEDs are shown to receive current densities in the range of 0.2 to 7 kA/cm^2, which, typically, places them in their droop regime (*26*, *27*).

Full three-dimensional finite-difference time-domain (FDTD) modeling (Fig. 4F) shows that the fin LEDs emit light from their facets open to air and have an intrinsic light extraction efficiency (LEE) of about 15%. The rest of the light is trapped in the *p*-GaN substrate due to a higher refractive index of GaN (2.5) relative to ZnO (2.2). The measured range of output power densities in Fig. 4E indicates that fin LEDs have the potential to exceed the power density of commercial planar UV-A LEDs of ≈23 to 75 W/cm^2 that are engineered to have greater than 85% LEEs (*21*, *42*). By increasing the LEE beyond 15%, we estimate up to five times increase in the brightness of fin-based light sources, for instance, by coupling them to waveguide modes or reducing the light trapping in the GaN slab. Reports on power measurements of individual nanowire LED pixels is scarce; however, recent measurements using ensembles of free-standing nanowire LEDs show power density values in the range of 0.001, 0.5, and 3 W/cm^2, respectively, for axial InGaN/GaN nanowires (*43*), InGaN/AlGaN dot-in-a-wire core-shell nanowires (*44*), and core-shell AlInGaN nanowires (*45*).

As the current density reaches above 50 mA (at about 500 kA/cm^2) in some of the fin LED pixels, the broad EL emission at 385 nm narrows to two intense lines at 403 and 417 nm. This is a clear indication of lasing. A representative example, presented in Fig. 5A, shows the spectral evolution of pixel #43 at different drive currents and appearance of the two sharp peaks at 100 mA. Similar lasing is seen in other pixels (fig. S3). In pixel #43, we observe a linear redshift in the EL peak positions as current is raised, similar to pixel #50 (Fig. 4C), which we attribute to the rise of the junction temperature (Fig. 5Bi). We note that pixel #43 with one fin shows 143 meV (16.5 nm) redshift in the EL peak at 50 mA, suggesting the junction temperature of approximately 340°C. The total radiant flux of pixel #43 during LED and lasing emissions, presented in Fig. 5Bii (red circles), shows the record output powers of 1.9 and 20 μW at 50 and 100 mA, respectively. The FWHM of the EL emission in Fig. 5Bii (purple

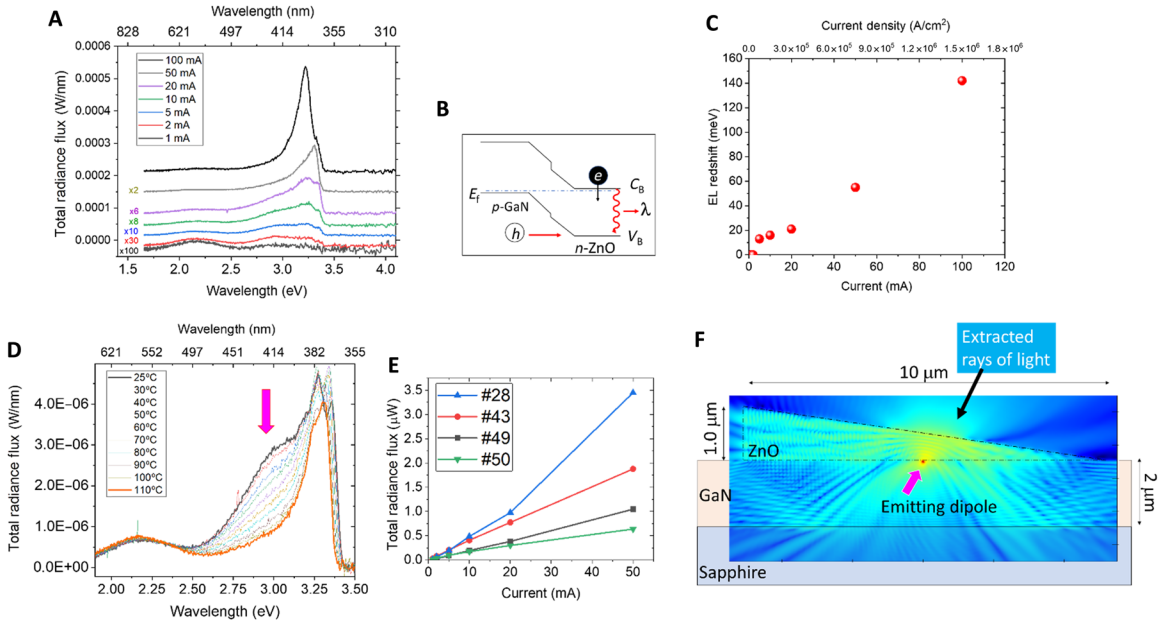

Fig. 4. EL of fin LEDs at high current density and heat. (**A**) Total spectral radiance flux (W/nm) of a representative pixel containing three fin LEDs as the injection current is raised from 1 to 100 mA. The acquisition time at each drive current is 50, 25, 10, 5, 2.5, 1, and 0.5 s, respectively. (**B**) ZnO-GaN band structure. (**C**) UV peak position redshifts (in eV) as current is increased. The expanded uncertainty of the measured peak position is less than 0.5 nm, with coverage factor of $k = 2$. (**D**) Change in EL of the fin LED pixel at a low current load of 2 mA as temperature increases from 25° to 110°C using a temperature-controlled stage. The broad emission at 420.2 nm (2.955 eV) due to *e-h* recombination in the GaN side does not redshift but is suppressed as temperature reaches 110°C. The intensity of the first UV emission related to *e-h* recombination in the ZnO fin at 368.5 nm (3.369 eV) stays almost the same but redshifts at 4.8 nm and nearly overlaps with the second UV peak. (**E**) Total radiant flux (output power) of four randomly selected fin LED pixels in the range of 1 to 3.5 μW (± 10%). (**F**) FDTD simulation of light extraction from a fin LED viewed from the long side of the fin. Dimensions are specified in the figure. A single dipole is oriented 45° at the interface. Light rays leave more from the tall sides of the fin. Model shows about 8% emission from sides and 7% from top.

diamonds) narrows from 65 to 2.7 nm once the device is pumped at 100 mA. This is 10 times increase in the output power due to a twofold increase in the injected current. Figure 5Ci compares the output power of this pixel (red circles) operating as a laser diode with other pixels as LEDs. If pixel #43 were an LED, then we would have expected only about a twofold increase in the output power as seen in pixel #50 of Fig. 5Ci (purple triangles). Similar to pixel #43, we observe an excellent consistency in lasing emission lines in other lasing pixels (such as pixels #28 and #49; fig. S3).

Our results suggest that a ZnO fin on GaN can act as a Fabry-Pérot cavity. Numerical modeling using three-dimensional FDTD technique shows the corresponding spectral response as measured in the far field when excited by a randomly oriented broadband dipole located at the interface between ZnO and GaN (fig. S4). Various passive cavity modes separated by the free spectral range (FSR) of approximately 14 to 16 nm in the cavity are consistent with the experimentally measured spacing between the two lasing modes (14 nm). Note that the experimentally observed FSR of 14 nm corresponds to an approximate cavity length of 2.5 μm (assuming a mode index of 2.4). The typical FWHM of the passive cavity modes is approximately 9 nm, corresponding to a quality factor ($Q = \lambda/\delta\lambda$) of the resonant mode of ≈45. This factor is limited primarily by the radiative losses (to free space and waveguiding in the GaN layer). By patterning the GaN layer around the nanofin, we expect the quality factor to improve by an order of magnitude. Upon electrically pumping the cavity above the lasing threshold, the two lasing modes at 403 and 417 nm appear (Fig. 5A). The decrease in linewidth from 9 to 2.7 nm upon lasing is consistent with that expected of a transition from the spontaneous emission to the stimulated emission regime. We believe that the lasing linewidth in the current configuration is both limited by the radiative losses (as discussed above) and by the nonradiative recombination due to high junction temperature. The ability of a fin with an approximate volume of 0.8 μm^3 to reach population inversion is quite notable, as droop effects and optical loss were expected to overwhelm the fin cavity for the junction temperature of about 340°C and 1000 kA/cm^2 current densities. Previous theoretical modeling has also suggested that the thermal effects can make nanoLED and nanolaser operation unsustainable beyond 100 kA/cm^2 (*11*).

To better understand the impact of *e-h* recombination pathways in fins, we investigated the wall-plug efficiency (WPE) of the fins in LED and lasing modes. Figure 5C (ii) shows the general trend in WPE for pixels in LED mode that has a rise followed by a decline, while for the lasing pixel (red circle), the WPE suddenly increases at 100 mA. The WPE (η_{WP}) of a fin LED is $\eta_{WP} = \eta_{INJ} \times \eta_{LEE} \times \eta_{IQE} \times \eta_{DRIVER}$, respectively, including current injection, LEE, IQE, and driver (feeding) efficiencies. The driver efficiency, $\eta_{DRIVER} \sim \frac{E_{gap}}{q V_{bias}}$, is the ratio of the mean energy of the photons emitted and the total energy that an electron-hole pair acquires from the power source. This value was calculated using the voltage-current scans of the fin LEDs (fig. S5) and used in the WPE equation above to extract the IQE dependences of the fin LED laser pixels as illustrated in the semi-log graph of Fig. 6A. As seen, the IQE of fin LED pixels does not show the efficiency droop even at very high current densities of 1000 kA/cm^2. Furthermore, the IQE shows an abrupt increase when the pixel becomes a laser diode. This is remarkable, as normally LEDs

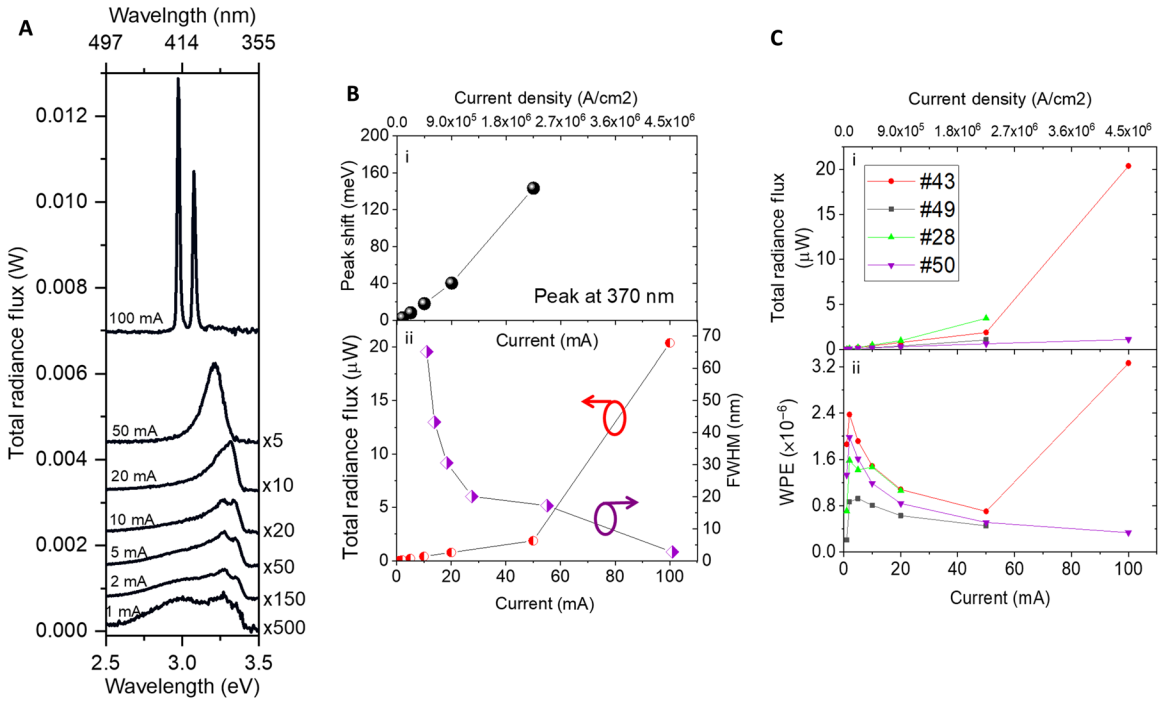

Fig. 5. Transition of fin LEDs to fin laser at high current density. (**A**) Total spectral radiant flux of fin LED pixel #43 in the range of 1 to 100 mA shows the EL spectral evolution. The acquisition time at each drive current is 65, 30, 5, 1, 0.5, 0.1, and 0.02 s, respectively. (**B**) (i) While pixel #43 is in the LED mode, the shift in EL peak position varies linearly as drive current is raised to 50 mA. (ii) Total radiant flux, in microwatt, output power (left axis) and EL linewidth narrowing (right axis) of pixel #43 in the range of 1 to 100 mA. (**C**) (i) Total radiant flux of pixel #43 (red), in microwatt, in LED and lasing modes and its comparison with three other LED pixels. (ii) WPE graphs of pixel #43 (red) in lasing mode and its comparison with three other LED pixels. In (B) and (C), current density in the upper part of the graph is for pixel #43.

show a strong decline in their IQE efficiency as current density increases. Experimentally measured WPE or EQE (external quantum efficiency) values for nanowire LEDs based on absolute radiant flux data are scarce. Earlier semiquantitative estimations in GaN-based nanowire LEDs show that EQE or IQE peaks at small injection currents ranging from 0.4 to 5 mA (*25*–*27*, *46*) correspond to current densities of 0.2 to 10 kA/cm^2. A more recent quantitative report on metal cavity InP-based nanopillar LEDs shows that about 22-nW power at maximum EQE of 10^{-4} is reached at a current range of 0.2 to 0.4 mA (current density of 100 kA/cm^2) (*17*). Because the fin design prevents the rollover in EQE, it is possible to achieve a comparable EQE of 6×10^{-5}, but at 40 times higher current densities. This advantage results in fin pixels with 1000 times more output power than that of the nanopillar LED design with one of the best reported performance.

As we discuss below, the heterodimensional fin architecture is conducive to limiting the droop effect and, therefore, helps in boosting IQE, which is a determining parameter in the overall performance of the LED. Another key factor for achieving high power emission and lasing is the high quality of ZnO crystal evidenced by the narrow bandwidth transitions observed by the CL and EL spectroscopies. To support this interpretation, we present a three-parameter (ABC) model based on the radiative and nonradiative processes including the SRH and Auger recombination (*47*), in which the energy is eventually released as heat. According to the ABC model (Supplementary Materials, eq. S1), IQE is given by

$$\eta = \frac{N_p}{1 + N_p + c_a N_p^2} \quad (1)$$

Here, $N_p = n/n_o$ is the dimensions electron-hole pair density, $n_o = \frac{A}{B}$, $c_a = CA/B^2$, and c_a is the dimensionless Auger recombination constant. This model (fig. S6) describes the impact of rise of nonradiative Auger recombination and decline of IQE. In the steady state, the current density flux gradient is estimated as $J = I/(qd)$, where $J = An + Bn^2 + Cn^3$. Here, I is the current density, q is the electron charge, and d is the characteristic length of the recombination region. The current density flux gradient (J) could be rewritten as $j = N_p + N_p^2 + c_a N_p^3$. Here, the dimensionless current flux density is $j = J/(An_o)$.

We consider two limiting cases: (i) the low injection regime, when the generation occurs close to the heterointerface (in this case, the Auger recombination is negligible), and (ii) high injection regime, when the generation occurs in the fin and the Auger recombination is dominant. In the low injection case, we neglect the Auger recombination contribution in the current flux density. In this case, the SRH defect–related carrier recombination is more dominant. However, it does not cause the efficiency droop. In the high injection regime, the Auger recombination is dominant, and the equation for the current flux density becomes $j = N_p + N_p^2 + c_a N_p^3 = c_a N_p^3$. In this regime

$$\eta_{high} = \frac{1}{c_a^{2/3} j^{1/3}} \quad (2)$$

This equation applies when $c_a N_p >> 1$ or $(jc_a^2)^{1/3} >> 1$. The general expression for IQE could be interpolated as

$$\eta = \frac{1}{1/\eta_{high} + 1/\eta_{low}} \quad (3)$$

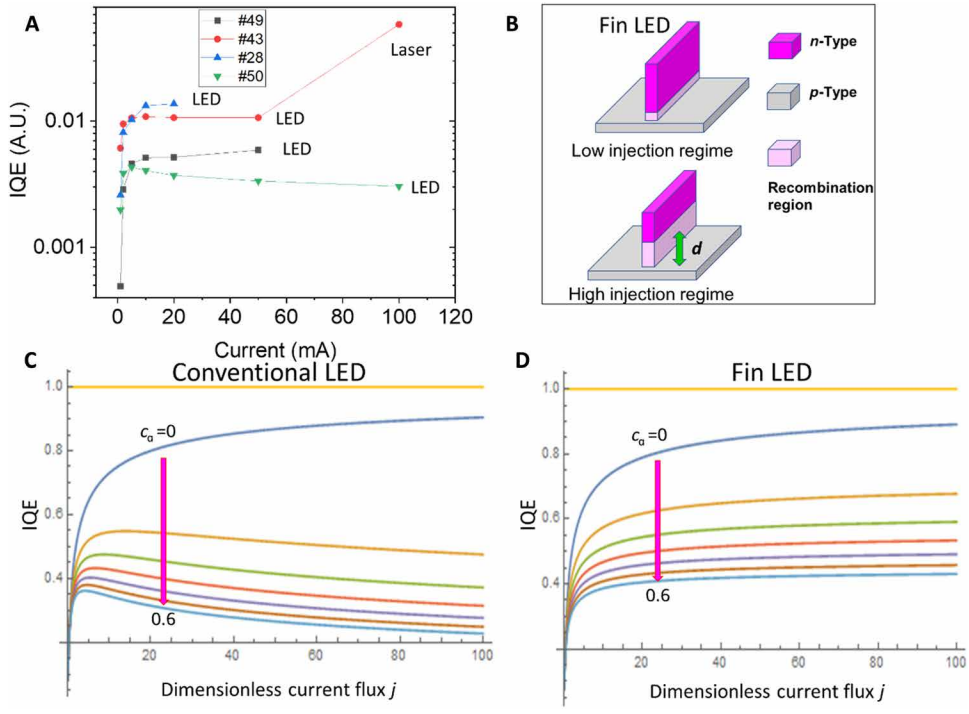

Fig. 6. IQE efficiencies of fin and planar LEDs. (**A**) IQE graph of pixel #43 (red) in LED and lasing modes and its comparison with three other LED pixels. The top scale presents the current density for pixel #43. (**B**) Fin LED charge spreading length "*d*" at low and high current injection regimes. (**C**) Calculated IQE versus dimensionless current flux *j* for conventional LEDs, from eq. S10 and eq. S3. The dimensionless Auger recombination constant c_a varies from 0 to 0.6 (step 0.1). (**D**) Calculated IQE versus dimensionless current flux *j* for fin LED, from eq. S13 and eq. S3. The dimensionless Auger recombination constant c_a varies from 0 to 0.6 (step 0.1). The parameter used in the calculation is the dimensionless injection current flux $j_o = 5$.

The key difference between the conventional LED and the fin LED is the dependence of current gradient *j* on the injection level. For conventional LEDs, the length of the recombination region, *d*, in the steady-state current density flux gradient, $J = I/(qd)$, is nearly independent of injected current, *I*. For the fin LEDs (Fig. 6B), *d* increases with *I* and the current gradient *j* saturates, leading to the saturation of the Auger recombination. For the conventional LED, we obtain the dependences shown in Fig. 6B. In this graph, as the Auger recombination constant c_a increases, the IQE declines (top to bottom curves). For the case of the fin LED, we assume that, at high injections, the electron hole pairs spread out, i.e., *d* increases (Fig. 6B). The reason for the recombination region expansion into the fin is the heterodimensional bottleneck effect occurring at the *n*-ZnO fin/*p*-GaN heterointerface. Because the current in the narrow fin must be equal to the current in the *p*-GaN region, the recombination length in the fin has to expand with the rising current to provide enough electrons to recombine with the holes collected from a much larger area. Consequently, the current gradient remains nearly constant with the rising current. The mathematics describing this current distribution is analogous to the problem of calculating the depletion region length for a heterodimensional (three-dimensional to two-dimensional) *p*-*n* junction (*48*). According to this model, the lasing occurs when the recombination region reaches the top of the fin and no longer expands with an increase in the injected current. For the high injection regime of a fin LED, Eqs. 2 and 3 predict nearly droop-free dependences shown in Fig. 6D.

We argue that both the SRH and Auger recombination pathways are mitigated in the ZnO fin architecture. At the low injection regime, when the generation occurs close to the heterointerface, the nonradiative SRH in ZnO is insignificant (Fig. 4D). Output power in Fig. 5C also show that, at high injection regime, when the generation occurs in the ZnO fin, the output power grows linearly with the injected current, indicating that carrier loss due to Auger recombination is minimal. The presented mechanism highlights the significance of the two factors stated above in improving the IQE at high current densities, namely, the fin shape facilitating the current gradient saturation and the high quality of ZnO crystal. In addition, ZnO fins do not host the threading dislocations originated at the underlying GaN substrate. This is due to their growth mechanism that governs the lateral growth in the surface-directed VLS process versus the epitaxy used for conventional planar LEDs. The ZnO-GaN thin film–based LEDs have shown the efficiency droop effect (*49*). Hence, ZnO is most likely not the critical compound for creating a droop-free LED. A ZnO fin, due to its sub–200-nm width, is expected to have a lower potential drop and resistive loss across its width (the two factors affecting the IQE). The comb-like structure of the *p*-GaN contact is also effective for the current spreading and for the effective hole injection into the fins.

Overall, the linear rise of the output power versus the injected current at high current densities shows the effectiveness of the fins in charge injection. Furthermore, the minimal impact of temperature on the defect-related SRH carrier loss in ZnO fin, at low injection current, underlines the low defect density of the fins. There is no electron-blocking layer in the presented fin heterojunction. Nevertheless, there is no detectable electron leakage and/or electron hole recombination in the *p*-GaN at high current densities. Our results

strongly indicate the absence or negligible presence of the critical factors that reduce the efficiency of conventional LEDs as well as submicrometer LEDs including electron leakage, Auger recombination, defect-related recombination, and temperature effects.

CONCLUSIONS

LEDs have been considered as the ideal lighting sources for a vast range of applications including residential, industrial, and automotive lighting; smart lighting; displays; visible light communications; biomedical applications; water and food sterilization; security systems; and sensors. Miniaturized LED and laser pixels with high-luminance/high-radiance point sources will revolutionize many of these applications including the advanced smart light sources in far-field applications such as multipixel LEDs and intelligent selective pixel control for use in smart lighting, display technology, and internet of things. NanoLEDs and nanolasers with a strongly reduced cavity volume have the potential to reach much higher modulation speeds for a wide range of near-field applications in sensing, metrology, microscopy, and on-chip communications. The main remaining challenge is that the existing nanoLEDs and nanolaser are too dim for most practical applications, with output powers in the nanowatts range, due to the dominance of temperature and current density droop effects. The architecture reported here is a simple fin ZnO-GaN LED with a submicrometer area that alleviates or removes these limitations. This design allows generation of output powers in the microwatt range, about 1000 times higher than that of existing nanoscale LEDs and lasers. We relate this enhanced performance to the impact of fin shape on mitigating the nonradiative pathways and providing large side facets for an effective electrical current injection and forming a laser cavity. Evidence of lasing in fin cavities with an estimated temperature well above room temperature further underlines the droop-free nature of the fins at extreme current densities. The findings here are highly encouraging and represent a significant step in designing architectures that can overcome the "current density droop" and "temperature droop" effects in LEDs to maximize their achievable output power per pixel. While the reported nanoLEDs and nanolasers operate in the near UV range, this concept could be applied to the materials system, such as AlGaN and BN, or to their heterostructures to develop far brighter deep UV LEDs and lasers. At microscale, these findings are expected to enable further reduction in the cavity size below sub–100 nm while offering high-performance and high-brightness light sources.

MATERIALS AND METHODS

Preparation of *n*-ZnO/*p*-GaN heterojunctions

The substrate for the lateral fin growth included a 200-nm-thick Mg-doped *p*-GaN epilayer on *c*-plane sapphire with an acceptor concentration of 5×10^{17} cm^{-3} (Kyma Technologies) (*50*). The *p*-GaN epilayer was grown on a 1500-nm, undoped GaN layer. GaN wafers were diced with a dicing saw to the 1-cm^2 dies. The wafer cleaning steps included solvent wash including hot acetone followed by isopropyl alcohol and drying with nitrogen gas.

Gold catalyst micropatterning

p-GaN substrates (1 cm^2) were photopatterned with a Karl Suss Mask aligner (*51*) with a nominal resolution of 2 μm. The Shipley 1813 photoresist layer was spin-casted according to the established clean room protocol. This layer was spun on the surface at 66.7 Hz (4000 rpm) in 45 s. After a 1-min bake at 115°C, it was patterned with catalyst micropatterns. The 10- to 20-nm-thick gold patterns were deposited using a thermal evaporator. Photoresist lift off was carried out in hot acetone followed by wash in warm and cold isopropyl alcohol.

Growth of ZnO nanofins

ZnO nanofins were grown on gold-patterned *p*-GaN surface using a modified surface-directed VLS growth process reported elsewhere. Growth was carried out in a horizontal tube furnace with a length of 800 mm and an inner diameter of 49 mm. The ZnO/graphite mixture of 0.140 g (1:1 mass ratio) was positioned at the center of a small quartz tube with a length of 130 mm and an inner diameter of 19 mm. The tube furnace temperature reached 890°C (with a ramp rate of ≈111°C per minute) and a dwell time of 40 min under ≈0.5 standard liters per minute (SLPM) flow of ultra-dry (99.99%) N_2 gas.

Measurement of optical power of fin LED and laser pixels

The fin LED chips were mounted on a temperature-controlled mount (TCM) through a metal core printed circuit board (MCPCB) (Fig. 3A). The fin LEDs were measured for total spectral radiant flux (W/nm) using a metrology-grade CCD array spectroradiometer with a spectral range from 300 to 1100 nm and a bandpass of 2.5 nm. The input optic of the spectroradiometer is the irradiance probe composed of a 44-mm-diameter integrating sphere with a 16-mm-diameter entrance port and a 5000-mm-long quartz optical fiber bundle with a 1.5-mm-diameter core. The spectroradiometer was corrected for spectral stray light errors using the method described elsewhere (*51*). Before the measurement of the fin LEDs, the spectroradiometer was calibrated for spectral irradiance responsivities. The calibration used a 1000-W spectral irradiance standard FEL lamp at 500 mm, and the spectroradiometer responsivity was converted to total spectral radiant flux responsivity by multiplying the spectral irradiance of the FEL lamp.

The fin LED chip was placed at the center of the entrance port and was less than 5 mm from the 16-mm-diameter entrance port so that the integrating sphere could collect more than 95% of light emitted by the LED. The errors resulting from the interreflection between the MCPCB of fin LEDs and the 16-mm-diameter entrance port of the integrating sphere were estimated to be less than 5%. The fin LEDs were measured for total spectral radiant flux at different operating current levels, and the spectroradiometer's integration time was adjusted accordingly, ranging from 65 to 0.02 s. The measured total spectral radiant flux (W/nm) was used to calculate the total radiant flux (W), covering the spectral range from 350 to 800 nm. The temperature of the TCM, where the device was mounted, was set to 25°C for all the measurements. The 10-min intervals between the consecutive measurements allowed the fin LED to reach its equilibrium temperature.

SUPPLEMENTARY MATERIALS

Supplementary material for this article is available at http://advances.sciencemag.org/cgi/content/full/6/33/eaba4346/DC1

REFERENCES AND NOTES

1. S. Nakamura, M. Senoh, T. Mukai, High-power InGaN/GaN double-heterostructure violet light emitting diodes. *Appl. Phys. Lett.* **62**, 2390–2392 (1993).
2. H. Amano, N. Sawaki, I. Akasaki, Y. Toyoda, Metalorganic vapor phase epitaxial growth of a high quality GaN film using an AlN buffer layer. *Appl. Phys. Lett.* **48**, 353–355 (1986).

3. H. Amano, M. Kito, K. Hiramatsu, I. Akasaki, P-type conduction in Mg-doped GaN treated with low-energy electron beam irradiation (LEEBI). *Jpn. J. Appl. Phys.* **28**, L2112–L2114 (1989).
4. A. Žukauskas, Color rendering metrics: Status, methods, and future development, in *Handbook of Advanced Lighting Technology*, R. Karlicek, C. C. Sun, G. Zissis, R. Ma, Eds. (Springer, 2016).
5. D. E. Mentley, State of flat-panel display technology and future trends. *Proc. IEEE* **90**, 453–459 (2002).
6. M. Shur, Wide band gap semiconductor technology: State-of-the-art. *Solid-State Electron.* **155**, 65–75 (2019).
7. I. Gaska, O. Bilenko, S. Smetona, Y. Bilenko, R. Gaska, M. Shur, Deep UV LEDs for public health applications. *Int. J. High Speed Electron. Syst.* **23**, 1450018 (2014).
8. S. Pleasants, Visible blind detector. *Nat. Photonics* **7**, 673–673 (2013).
9. V. S. Chivukula, D. Ciplys, R. Rimeika, M. S. Shur, J. Yang, R. Gaska, Impact of photocapacitance on phase response of GaN/Sapphire SAW UV sensor. *IEEE Sens. J.* **10**, 883–887 (2010).
10. M. Shur, Terahertz technology: Devices and applications, in *Proceedings of the 31st European Solid-State Circuits Conference, 2005. ESSCIRC 2005* (IEEE, 2005), pp. 13–21.
11. B. Romeira, A. Fiore, Physical limits of NanoLEDs and nanolasers for optical communications. *Proc. IEEE*, 1–14 (2019).
12. R.-M. Ma, R. F. Oulton, Applications of nanolasers. *Nat. Nanotechnol.* **14**, 12–22 (2019).
13. E. Luan, H. Shoman, D. M. Ratner, K. C. Cheung, L. Chrostowski, Silicon photonic biosensors using label-free detection. *Sensors* **18**, 3519 (2018).
14. C. Liao, Y.-F. Chang, C.-L. Ho, M.-C. Wu, Y.-T. Hsieh, C.-Y. Li, M.-P. Houng, C.-F. Yang, Light-emitting diodes for visible light communication, in *2015 International Wireless Communications and Mobile Computing Conference (IWCMC)* (IEEE, 2015), pp. 665–667.
15. G. Shambat, B. Ellis, A. Majumdar, J. Petykiewicz, M. A. Mayer, T. Sarmiento, J. Harris, E. E. Haller, J. Vučković, Ultrafast direct modulation of a single-mode photonic crystal nanocavity light-emitting diode. *Nat. Commun.* **2**, 539 (2011).
16. H.-G. Park, S. H. Kim, S. H. Kwon, Y. G. Ju, J. K. Yang, J. H. Baek, S. B. Kim, Y. H. Lee, Electrically driven single-cell photonic crystal laser. *Science* **305**, 1444 (2004).
17. V. Dolores-Calzadilla, B. Romeira, F. Pagliano, S. Birindelli, A. Higuera-Rodriguez, P. J. van Veldhoven, M. K. Smit, A. Fiore, D. Heiss, Waveguide-coupled nanopillar metal-cavity light-emitting diodes on silicon. *Nat. Commun.* **8**, 14323 (2017).
18. K. Ding, M. T. Hill, Z. C. Liu, L. J. Yin, P. J. van Veldhoven, C. Z. Ning, Record performance of electrical injection sub-wavelength metallic-cavity semiconductor lasers at room temperature. *Opt. Express* **21**, 4728–4733 (2013).
19. X. Duan, Y. Huang, R. Agarwal, C. M. Lieber, Single-nanowire electrically driven lasers. *Nature* **421**, 241–245 (2003).
20. K. H. Li, X. Liu, Q. Wang, S. Zhao, Z. Mi, Ultralow-threshold electrically injected AlGaN nanowire ultraviolet lasers on Si operating at low temperature. *Nat. Nanotechnol.* **10**, 140–144 (2015).
21. M. R. Krames, O. B. Shchekin, R. Mueller-Mach, G. O. Mueller, L. Zhou, G. Harbers, M. G. Craford, Status and future of high-power light-emitting diodes for solid-state lighting. *J. Display Technol.* **3**, 160–175 (2007).
22. D. S. Meyaard, Q. Shan, J. Cho, E. F. Schubert, S. H. Han, M. H. Kim, C. Sone, S. J. Oh, J. K. Kim, Temperature dependent efficiency droop in GaInN light-emitting diodes with different current densities. *Appl. Phys. Lett.* **100**, 081106 (2012).
23. S. Watanabe, N. Yamada, M. Nagashima, Y. Ueki, C. Sasaki, Y. Yamada, T. Taguchi, K. Tadatomo, H. Okagawa, H. Kudo, Internal quantum efficiency of highly-efficient InxGa1−xN-based near-ultraviolet light-emitting diodes. *Appl. Phys. Lett.* **83**, 4906–4908 (2003).
24. K. Fujiwara, H. Jimi, K. Kaneda, Temperature-dependent droop of electroluminescence efficiency in blue (In,Ga)N quantum-well diodes. *Phys. Status Solidi C* **6**, S814–S817 (2009).
25. I. M. Høiaas, A. Liudi Mulyo, P. E. Vullum, D. C. Kim, L. Ahtapodov, B. O. Fimland, K. Kishino, H. Weman, GaN/AlGaN Nanocolumn ultraviolet light-emitting diode using double-layer graphene as substrate and transparent electrode. *Nano Lett.* **19**, 1649–1658 (2019).
26. B. Janjua, H. Sun, C. Zhao, D. H. Anjum, F. Wu, A. A. Alhamoud, X. Li, A. M. Albadri, A. Y. Alyamani, M. M. El-Desouki, T. K. Ng, B. S. Ooi, Self-planarized quantum-disks-in-nanowires ultraviolet-B emitters utilizing pendeo-epitaxy. *Nanoscale* **9**, 7805–7813 (2017).
27. Y.-H. Ra, R. Wang, S. Y. Woo, M. Djavid, S. M. Sadaf, J. Lee, G. A. Botton, Z. Mi, Full-color single nanowire pixels for projection displays. *Nano Lett.* **16**, 4608–4615 (2016).
28. Y. C. Shen, G. O. Mueller, S. Watanabe, N. F. Gardner, A. Munkholm, M. R. Krames, Auger recombination in InGaN measured by photoluminescence. *Appl. Phys. Lett.* **91**, 141101 (2007).
29. J. Iveland, L. Martinelli, J. Peretti, J. S. Speck, C. Weisbuch, Direct measurement of auger electrons emitted from a semiconductor light-emitting diode under electrical injection: Identification of the dominant mechanism for efficiency droop. *Phys. Rev. Lett.* **110**, 177406 (2013).
30. G. Bourdon, I. Robert, I. Sagnes, I. Abram, Spontaneous emission in highly excited semiconductors: Saturation of the radiative recombination rate. *J. Appl. Phys.* **92**, 6595–6600 (2002).
31. J. Mickevičius, J. Jurkevičius, G. Tamulaitis, M. S. Shur, M. Shatalov, J. Yang, R. Gaska, Influence of carrier localization on high-carrier-density effects in AlGaN quantum wells. *Opt. Express* **22**, A491–A497 (2014).
32. J. Mickevičius, J. Jurkevičius, M. S. Shur, J. Yang, R. Gaska, G. Tamulaitis, Photoluminescence efficiency droop and stimulated recombination in GaN epilayers. *Opt. Express* **20**, 25195–25200 (2012).
33. J. Wang, L. Wang, W. Zhao, Z. Hao, Y. Luo, Understanding efficiency droop effect in InGaN/GaN multiple-quantum-well blue light-emitting diodes with different degree of carrier localization. *Appl. Phys. Lett.* **97**, 201112 (2010).
34. S. Hammersley, D. Watson-Parris, P. Dawson, M. J. Godfrey, T. J. Badcock, M. J. Kappers, C. McAleese, R. A. Oliver, C. J. Humphreys, The consequences of high injected carrier densities on carrier localization and efficiency droop in InGaN/GaN quantum well structures. *J. Appl. Phys.* **111**, 083512 (2012).
35. J. Mickevičius, G. Tamulaitis, M. Shur, M. Shatalov, J. Yang, R. Gaska, Correlation between carrier localization and efficiency droop in AlGaN epilayers. *Appl. Phys. Lett.* **103**, 011906 (2013).
36. N. I. Bochkareva, Y. T. Rebane, Y. G. Shreter, Efficiency droop and incomplete carrier localization in InGaN/GaN quantum well light-emitting diodes. *Appl. Phys. Lett.* **103**, 191101 (2013).
37. N. I. Bochkareva, Y. T. Rebane, Y. G. Shreter, Efficiency droop in GaN LEDs at high current densities: Tunneling leakage currents and incomplete lateral carrier localization in InGaN/GaN quantum wells. *Sem. Ther.* **48**, 1079–1087 (2014).
38. A. Janotti, C. G. Van de Walle, Fundamentals of zinc oxide as a semiconductor. *Rep. Prog. Phys.* **72**, 126501 (2009).
39. B. Nikoobakht, A. Herzing, Formation of planar arrays of one-dimensional p–n heterojunctions using surface-directed growth of nanowires and nanowalls. *ACS Nano* **4**, 5877–5886 (2010).
40. M. A. Zimmler, T. Voss, C. Ronning, F. Capasso, Exciton-related electroluminescence from ZnO nanowire light-emitting diodes. *Appl. Phys. Lett.* **94**, 241120 (2009).
41. J. Piprek, Efficiency droop in nitride-based light-emitting diodes. *Phys. Status Solidi A* **207**, 2217–2225 (2010).
42. Y. Narukawa, M. Ichikawa, D. Sanga, M. Sano, T. Mukai, White light emitting diodes with super-high luminous efficacy. *J. Phys. D Appl. Phys.* **43**, 354002 (2010).
43. A. L. Bavencove, G. Tourbot, J. Garcia, Y. Désières, P. Gilet, F. Levy, B. André, B. Gayral, B. Daudin, L. S. Dang, Submicrometre resolved optical characterization of green nanowire-based light emitting diodes. *Nanotechnology* **22**, 345705 (2011).
44. H. P. T. Nguyen, M. Djavid, S. Y. Woo, X. Liu, A. T. Connie, S. Sadaf, Q. Wang, G. A. Botton, I. Shih, Z. Mi, Engineering the carrier dynamics of InGaN nanowire white light-emitting diodes by distributed p-AlGaN electron blocking layers. *Sci. Rep.* **5**, 7744 (2015).
45. R. Wang, X. Liu, I. Shih, Z. Mi, High efficiency, full-color AlInGaN quaternary nanowire light emitting diodes with spontaneous core-shell structures on Si. *Appl. Phys. Lett.* **106**, 261104 (2015).
46. M. Nami, I. E. Stricklin, K. M. DaVico, S. Mishkat-Ul-Masabih, A. K. Rishinaramangalam, S. R. J. Brueck, I. Brener, D. F. Feezell, Carrier dynamics and electro-optical characterization of high-performance GaN/InGaN core-shell nanowire light-emitting diodes. *Sci. Rep.* **8**, 501 (2018).
47. S. Karpov, *Numerical Simulation of Optoelectronic Devices, 2014*. (IEEE, 2014), pp. 17–18.
48. B. Gelmont, M. Shur, C. Moglestue, Theory of junction between two-dimensional electron gas and p-type semiconductor. *IEEE Trans. Electron Dev.* **39**, 1216–1222 (1992).
49. S. Jeong, H. Kim, Enhanced performance characteristics of n-ZnO/p-GaN heterojunction light-emitting diodes by forming excellent Ohmic contact to p-GaN. *Mater. Sci. Semicond. Process.* **39**, 771–774 (2015).
50. Certain commercial equipment, instruments, materials, or software are identified in this paper to foster understanding. Such identification does not imply recommendation or endorsement by the National Institute of Standards and Technology, nor does it imply that the materials or equipment identified are necessarily the best available for the purpose.
51. Y. Zong, S. W. Brown, B. C. Johnson, K. R. Lykke, Y. Ohno, Simple spectral stray light correction method for array spectroradiometers. *Appl. Optics* **45**, 1111–1119 (2006).

Acknowledgments: We would like to thank C. B. Montgomery at the Biomolecular Measurement Division of NIST for his support and for performing the wire bonding related to this project. **Funding:** A.A. acknowledges support under the Cooperative Research Agreement between the University of Maryland and the National Institute of Standards and Technology, Center for Nanoscale Science and Technology, award no. 70NANB14H209, through the University of Maryland. The work at RPI was supported by the U.S. Army Cooperative Research Agreement. **Author contributions:** B.N. conceived and oversaw the experiments. Y.Z. designed the EL measurement setup. Y.Z. and B.N. conducted the EL measurements. R.P.H.

fabricated the LED device. M.S. provided the theoretical model. A.A. performed the optical modeling. J.T. assisted in analyzing data and improving the fin growth. B.N. wrote the manuscript with help of J.T., M.S., and other authors. **Competing interests:** B.N. and R.P.H. are authors on a patent application related to this work submitted by the National Institute of Standards and Technology (no. 16/804,203, filed on 28 February 2020). The authors declare no other competing interests. **Data and materials availability:** All data needed to evaluate the conclusions in the paper are present in the paper and/or the Supplementary Materials. Additional data related to this paper may be requested from the authors.

Submitted 4 December 2019
Accepted 2 July 2020
Published 14 August 2020
10.1126/sciadv.aba4346

Citation: B. Nikoobakht, R. P. Hansen, Y. Zong, A. Agrawal, M. Shur, J. Tersoff, High-brightness lasing at submicrometer enabled by droop-free fin light-emitting diodes (LEDs). *Sci. Adv.* **6**, eaba4346 (2020).

Science Advances

High-brightness lasing at submicrometer enabled by droop-free fin light-emitting diodes (LEDs)

Babak Nikoobakht, Robin P. Hansen, Yuqin Zong, Amit Agrawal, Michael Shur and Jerry Tersoff

Sci Adv **6** (33), eaba4346.
DOI: 10.1126/sciadv.aba4346